Nanoscale

Near-Infrared Optical Transitions in PdSe2 Phototransistors

Journal:	*Nanoscale*
Manuscript ID	NR-ART-04-2019-003505.R1
Article Type:	Paper
Date Submitted by the Author:	17-Jun-2019
Complete List of Authors:	Walmsley, Thayer; Vanderbilt University, Electrical Engineering and Computer Science Andrews, Kraig; Wayne State University, Wang, Tianjiao; Vanderbilt University, Electrical Engineering and Computer Science Haglund, Amanda; University of Tennessee Knoxville, Materials Science and Engineering Rijal, Upendra; Wayne State University Bowman, Arthur; Wayne State University Mandrus, David; University of Tennessee, Department of Materials Science and Engineering Zhou, Zhixian; Wayne State University Xu, Yaqiong; Vanderbilt University, Electrical Engineering and Computer Science

Near-Infrared Optical Transitions in $PdSe_2$ Phototransistors

Thayer S. Walmsley[1], Kraig Andrews[2], Tianjiao Wang[3], Amanda Haglund,[4] Upendra Rijal,[2] Arthur Bowman,[2] David Mandrus,[4,5] Zhixian Zhou[,2], and Ya-Qiong Xu[*,1,3]*

[1]Department of Physics and Astronomy, Vanderbilt University, Nashville, TN 37235, USA

[2]Department of Physics and Astronomy, Wayne State University, Detroit, MI 48201, USA

[3]Department of Electrical Engineering and Computer Science, Vanderbilt University, Nashville, TN 37235, USA

[4]Department of Materials Science and Engineering, University of Tennessee, Knoxville, TN 37235, USA

[5]Materials Science and Technology Division, Oak Ridge National Laboratory, Oak Ridge, TN 37831, USA

*Correspondence to: yaqiong.xu@vanderbilt.edu and zxzhou@wayne.edu

Abstract

We investigate electronic and optoelectronic properties of few-layer palladium diselenide ($PdSe_2$) phototransistors through spatially-resolved photocurrent measurements. A strong photocurrent resonance peak is observed at 1060 nm (1.17 eV), likely attributed to indirect optical transitions in few-layer $PdSe_2$. More interestingly, when the thickness of $PdSe_2$ flakes increases, more and more photocurrent resonance peaks appear in the near-infrared region, suggesting strong interlayer interactions in few-layer $PdSe_2$ help open up more optical transitions between the conduction and valence bands of $PdSe_2$. Moreover, gate-dependent measurements indicate that remarkable photocurrent responses at the junctions between $PdSe_2$ and metal electrodes primarily result from the photovoltaic effect when a $PdSe_2$ phototransistor is in the off-state and are partially attributed to the photothermoelectric effect when the device turns on. We also demonstrate $PdSe_2$ devices with a Seebeck coefficient as high as 74 μV/K at room temperature, which is comparable with recent theoretical predications. Additionally, we find that the rise and decay time constants of $PdSe_2$ phototransistors are ~156 μs and ~163 μs, respectively, which are more than three orders of magnitude faster than previous $PdSe_2$ work and two orders of magnitude over other noble metal dichalcogenide phototransistors, offering new avenues for engineering future optoelectronics.

Keywords: $PdSe_2$, photocurrent, indirect transition, response time, TMDs

Introduction

Despite the diverse array of electrical, mechanical, and optical properties in graphene, the lack of a sizeable band gap has limited its ability to be used in some electronic and optoelectronic applications.[1, 2] The unique structure as well as the extraordinary physical properties of graphene, owing largely to its two-dimensional (2D) nature, has generated intense interest to find other 2D materials with an appreciable band gap. One such class of materials is the transition metal dichalcogenide (TMD) family. These materials are characterized by the X−M−X structure, where the X represents a chalcogen atom (primarily S, Se, Te), and the M is a transition metal from groups IV through VII or X. Though many TMDs are well understood in their bulk form, relatively few have received significant attention in their few-layer or monolayer form. The recent foray into the atomic thickness scale for these materials have revealed semiconductors (MoS_2, WSe_2, etc.), semimetals (WTe_2, etc.) and metals (VSe_2, etc.).[3-5] The most notable and perhaps most studied 2D materials beyond graphene are group-VI TMDs such as MoS_2, $MoSe_2$, and WSe_2, which have shown fantastic electronic,[6, 7] optoelectronic,[8, 9] and valleytronic properties.[10, 11] The success of these materials has led to the exploration of other transition metals to form these compounds. Among group-VII TMDs, a high external quantum efficiency and a thickness-independent band gap of ReS_2 make it an attractive candidate for optoelectronics.[12] Additionally, a novel structure with mirror-symmetric single-crystal domains has been shown in monolayer $ReSe_2$ and is suggestive of novel anisotropic electronic and optoelectronic properties.[13]

More recently, the exploration of group-X TMDs (noble metal dichalcogenides) has begun. Excellent near-infrared (NIR) photodetection capabilities have been

demonstrated in $PtSe_2$ field-effect transistors (FETs).[14] And an ultrahigh photogain has been achieved in back-gate modulated PtS_2 devices.[15] Of particular interest from this class of materials is $PdSe_2$. The high theoretically predicted mobility, an order of magnitude higher than Black Phosphorous (BP),[16] air stability of the electronic properties, and thickness-dependent band gap ranging from ~ 0 eV in bulk to an indirect band gap of ~1.43 eV in a monolayer structure make it an interesting material to further probe its optoelectronic properties.[17-19] Furthermore, the unique buckled pentagonal structure of $PdSe_2$ makes it a highly intriguing and desirable 2D material due to the resulting low-symmetry lattice structure. With the dominance of the hexagonal arrangement of atoms in popular 2D materials such as in MoS_2 and graphene or the buckled hexagonal arrangement of atoms in BP, the novel structure present in $PdSe_2$ offers many interesting opportunities.[16-23]

In this study, electrical transport and optoelectronic measurements are performed on few-layer $PdSe_2$ phototransistors via scanning photocurrent microscopy. Our experimental results suggest that the strong photocurrent signals at metal-$PdSe_2$ junctions are mainly attributed to the photovoltaic effect (PVE) when $PdSe_2$ phototransistors turn off and partially related to the photothermoelectric effect (PTE) when the devices are in the on-state. We also demonstrate $PdSe_2$ devices with a Seebeck coefficient as high as 74 μV/K at room temperature, which is consistent with theoretical predications.[18, 20] More importantly, thickness-dependent photoresponse resonance peaks are observed in the NIR region, which likely results from indirect optical transitions in few-layer $PdSe_2$. Additionally, a fast response time is obtained (~156 μs), which is an improvement of more than two orders of magnitude over previous reports for other TMD phototransistors

and a three order of magnitude improvement over previous $PdSe_2$ work.[12, 13, 15, 23, 24] This work offers new insight into the optoelectronic properties of $PdSe_2$ and opens up new avenues for engineering future 2D noble metal dichalcogenide based electronics and optoelectronics.

Results and Discussion

High-quality few-layer $PdSe_2$ flakes were mechanically exfoliated from a bulk crystal, and subsequently transferred to degenerately-doped Si substrates covered with a 270 nm SiO_2 layer. Thin $PdSe_2$ flakes (5-20 nm) were then identified by using optical microscopy and characterized with a Park-Systems XE-70 non-contact atomic force microscope (AFM). Finally, metal electrodes were fabricated onto the flakes by using standard electron-beam lithography and subsequent deposition of 10 nm Ti and 45 nm Au to create FETs where the degenerately-doped Si substrate was used as the back gate. Figures 1a and 1b show a schematic and an optical micrograph, respectively, of an as-fabricated typical $PdSe_2$ transistor. The gold electrodes and few-layer $PdSe_2$ are outlined in gray and purple dashed lines, respectively. Electrical properties of the devices were measured in a Janis ST-500 Microscopy Cryostat under high vacuum (~ 10^{-6} Torr). Figure 1c displays the gate-dependent electrical transport characteristics of a 9 nm (~ 15 layer) thick $PdSe_2$ transistor at room temperature. The device exhibits a predominately n-type behavior with an on/off ratio greater than ~ 10^4, which is better than or comparable to a previous report.[21] The field-effect electron mobility of the device was calculated to be ~ $92\ cm^2V^{-1}s^{-1}$ at room temperature by using the expression of $\mu_{FET} = {}^{L}/_{W} \times {}^{1}/_{C_{bg}} \times {}^{dG}/_{dV_G}$, where L and W are the length and width of the channel, respectively; C_{bg} is the capacitance of the Si back gate; G is the conductance; and ${}^{dG}/_{dV_G}$ is the slope

of the G-V_G curve in the linear region. Although the field-effect mobility observed in this device is significantly lower than theoretical predictions,[16, 17] it is comparable to or better than other experimental measurements.[21, 23] The observed field-effect mobility of the $PdSe_2$ device is likely limited by the presence of a substantial Schottky barrier (~ 180 meV) at the electrical contacts (see Figure S1 of the Supporting Information). The linear output characteristic of the $PdSe_2$ device for gate voltages sweeping from -80 V to 80 V, as shown in Figure 1d, can be attributed to thermally assisted tunneling through the Schottky barrier.[25]

To investigate the photoresponse of the $PdSe_2$ device, spatially-resolved photocurrent measurements were performed in an Olympus microscopy setup. A continuous wave laser beam (NKT Photonics SuperK Supercontinuum Laser) was expanded and then focused by a 40X Olympus objective (N.A. = 0.6) into a diffraction-limited spot (~ 1 μm) and scanned over the device using piezo-controlled mirrors with nanometer-scale spatial resolution. Figure 2b shows the scanning photocurrent image of the $PdSe_2$ device under 1060 nm illumination at zero gate and zero drain-source bias, whose corresponding reflection image was recorded simultaneously (Figure 2a). The electrodes and $PdSe_2$ are outlined in gray and purple dashed lines, respectively. Strong photocurrent signals ($I_{pc} = I_{laser} - I_{dark}$) observed at the metal-$PdSe_2$ junctions are likely due to the creation of potential barriers from the Fermi level alignment at the junctions, which results in built-in electric fields that can efficiently separate photo-excited electron-hole pairs (EHPs) to generate photocurrent signals.[26]

Furthermore, wavelength-dependent scanning photocurrent measurements were taken to investigate the photocurrent generation mechanisms in few-layer $PdSe_2$. Figure 2c shows photocurrent responses of the $PdSe_2$ devices with different thicknesses. For

thinner $PdSe_2$ phototransistors (e.g. 9 layers), a dominant resonance peak was observed at 1060 nm (1.17 eV), which is comparable to the indirect band gap of bi-layer $PdSe_2$ revealed by scanning tunneling spectroscopy (1.15 ± 0.07 eV).[27] Interestingly, when the thickness of $PdSe_2$ increases, more small peaks emerge around this near-IR region, such as peaks located at 1030 nm (1.20 eV) and 1090 nm (1.14 eV), respectively. These distinct peaks are likely attributed to different optical transitions between the local valence band maxima along the Γ-X line and the local conduction band minima located at the Γ-M line,[19] which are affected by the thickness due to the strong interlayer coupling in the puckered pentagonal morphology of $PdSe_2$.[28] This may also explain the uncertainty of the few-layer $PdSe_2$ band gap characterization in previous optical absorption measurements (0.7 – 1.3 eV).[17]

To further study the photocurrent generation mechanisms, gate-dependent scanning photocurrent measurements were performed by sweeping the gate voltage from -80 V to 0 V while recording the photocurrent along the $PdSe_2$ channel (Figure 2d). The photocurrent signal exhibits monotonic gate voltage dependence in the off-state (Figure 2e), indicating that the PVE plays an important role in its photocurrent generation. Upon laser excitation, EHPs will be generated locally and driven in opposite directions by the built-in electric field owing to the Fermi level alignment that leads to Schottky barriers at metal-$PdSe_2$ junctions. Since the electronic energies are higher near the metal contacts than those in the middle of the $PdSe_2$ channel when the device is electrostatically n-doped (Figure 2f, right), photo-excited electrons will be injected into the channel, leading to a negative/positive current flow in the drain/source electrode. The center of the channel shows negligible photocurrent response due to the relatively flat band structure at this

location. When V_G decreases to -44 V, flat band condition is reached (Figure 2f, middle), resulting in negligible photocurrent response. Similarly, an opposite polarity of photocurrent response is observed when the device is operating in the p-type region (Figure 2f, left).

Interestingly, the photocurrent signals start to saturate when V_G is larger than -20 V (Figure 2e), which can be attributed to reduced gate-tunability of the band bending in the depletion regions as the Fermi level approaches the conduction band edge. In addition to photovoltaic mechanisms, other photocurrent generation mechanisms may also contribute to the photocurrent. Under illumination, the laser beam can also locally heat $PdSe_2$ to produce photocurrent response via either the photo-bolometric effect (PBE) or the PTE. When a laser beam scans over a $PdSe_2$ channel, the temperature of the channel increases due to light-induced heating, leading to the electrical conductance increase of the channel (Figure. S2a).[29, 30] Therefore, PBE-induced photocurrent scales linearly with the drain-source bias. As shown in Figure S2b, the photocurrent response does not scale linearly with the drain-source bias, suggesting that the PTE may also contribute to the photocurrent generation. To further study the photocurrent generation mechanisms in metal-$PdSe_2$ junctions, we look into the spatially-resolved scanning photocurrent images of the $PdSe_2$ device. As shown in Figure S2c, a strong photocurrent "tail" is observed in the metal-$PdSe_2$ junction region, indicating that PTE also contributes to the photocurrent generation.[31, 32] Since the Seebeck coefficients of $PdSe_2$ (S_1) and the gold electrodes (S_2) are different, a photothermal voltage (V_{PTE}) across the metal-$PdSe_2$ junction exists:

$$V_{PTE} = (S_1 - S_2)\Delta T \quad (1).$$

From the Mott relation,[32-34] we can obtain the Seebeck coefficient from

$$S = -\frac{\pi^2 k_b^2 T}{3e} \frac{1}{G} \frac{dG}{dV_G} \frac{dV_G}{dE}\Bigg|_{E=E_F} \quad (2).$$

where k_b is the Boltzmann constant, T is the temperature, e is the charge of an electron, and E_F is the Fermi energy. Here, the $\frac{dV_G}{dE}\Big|_{E=E_F}$ can be estimated as follows. When the Fermi level moves from the valence band to the conduction band, the barrier height E_b (the energy from the Fermi level to the valence band) changes linearly with V_G ($\delta E_b = e\alpha\delta V_G$), where α is a numerical constant that measures how effectively the gate voltage modulates the band energy.[26, 35] The measured shut-off gate voltages for p-type and n-type conductance are -60 V and -20 V, respectively (Figure 1b). The band gap for few-layer $PdSe_2$ is 1.17 eV; therefore, the calculated $\alpha \approx 0.029$ can be used to infer the Seebeck coefficient. We obtained the maximum Seebeck coefficient of $PdSe_2$ (~ 74 μV/K at V_G = -10 V), which is consistent with the theoretically-predicted value of ~ 200 μV/K.[20] Therefore, photocurrent signals of $PdSe_2$ in the on-state may partially result from the PTE. Additionally, we performed power-dependent photocurrent measurements for the $PdSe_2$ device. As shown in Figure 2g, the photocurrent signals have a nearly linear relationship with incident power ($I_{PC} \sim P^{0.85}$). A linear relationship is expected due to the increased generation of EHPs with increased number of incident photons. The slight deviation from the linear relationship may result from some defects and trap states in the $PdSe_2$ channel.[8, 13, 36]

Next, we performed bias-dependent scanning photocurrent measurements on the $PdSe_2$ phototransistors at zero gate and different drain-source biases from -150 mV to 150 mV (Figure 3a). Here the electrodes and few-layer $PdSe_2$ channel are outlined in gray and purple dashed lines, respectively. Regardless of the applied bias, strong

photocurrent signals are observed at the metal-$PdSe_2$ junctions while the photocurrent response in the middle of the $PdSe_2$ channel is negligible. For comparison, corresponding horizontal cut lines along the channel (dashed lines in Figure 3a) are shown in Figure 3b. When a large positive bias is applied to the device, the positive photocurrent intensity at the source contact electrode increases. Similarly, the negative photocurrent signal in the drain contact electrode intensifies as the device is negatively biased. This increase in photoresponse under the application of a larger bias is primarily due to the enhancement of the electric field in the depletion region at the electrical contacts, which allows for more efficient separation and collection of the photo-excited EHPs. Since the slope of the electrostatic potential (or the local electric field) is roughly proportional to the photocurrent intensity, we numerically integrated the photocurrent curves in Figure 3b to obtain the electrostatic potential (Figure 3c). The potential change in different regions at various biases can be easily identified. Large potential drops near the electrode contact regions and relatively flat band in the middle of the $PdSe_2$ channel are observed, indicating the presence of contact resistances due to the Schottky barriers between metal electrodes and the $PdSe_2$ channel. By selecting electrode metals with proper work functions and eliminating (or reducing) the Fermi level pinning, the Schottky barrier between electrode contacts and the $PdSe_2$ channel may be minimized.[37-39]

We also study the photoresponse dynamics of $PdSe_2$ phototransistors through time-resolved scanning photocurrent measurements. In our experiment, an optical chopper was added to the system to apply ON/OFF light modulation while photocurrent signals were recorded as a function of time in order to measure the rise and decay time constants, as shown in Figure 4a. The rectangular excitation pulse generated by the

chopper has a width of ~ 2 ms with a rise time of ~100 ns. The device performed similarly over thousands of cycles of ON/OFF light modulation signifying the stability of the temporal response of the device. Figure 4b shows three typical cycles. By applying a single exponential function to fit the rising and decaying regions of the curve, the obtained rise and decay time constants are ~ 156 μs and ~ 163 μs (Figure 4c), respectively, which are more than three orders of magnitude faster than previous $PdSe_2$ work and two orders of magnitude over other group-X TMD devices.[12, 13, 15, 23, 24] These extremely fast response times are likely attributed to the high mobility of charge carriers in $PdSe_2$.[16, 40]

Conclusion

Through electrical transport and scanning photocurrent measurements, we demonstrate that strong photocurrent responses in $PdSe_2$ phototransistors primarily result from the PVE when the devices turn off and are partially related to the PTE when the devices are in the on-state. We also show $PdSe_2$ devices with Seebeck coefficients as high as 74 μV/K at room temperature, which is consistent with theoretical predications. Moreover, thickness-dependent photocurrent resonance peaks are observed in the NIR region, which are likely attributed to the strong interlayer coupling-induced indirect optical transitions in few-layer $PdSe_2$. Additionally, a fast response time of ~ 156 μs has been achieved in $PdSe_2$ phototransistors, which is more than three orders of magnitude faster than previous report and two orders of magnitude over other noble metal dichalcogenide devices. This work not only presents new insight into the optical transitions and photocurrent generation mechanisms of $PdSe_2$, but also opens up new avenues for engineering future noble metal dichalcogenide based optoelectronic devices.

Acknowledgements

This work was supported by the National Science Foundation (ECCS-1810088 and CBET-1805924). A.H. and D.M. acknowledge support from the Gordon and Betty Moore Foundation's EPiQS Initiative Grant No. GBMF4416.

Additional Information

The authors declare no competing financial interests.

Figures

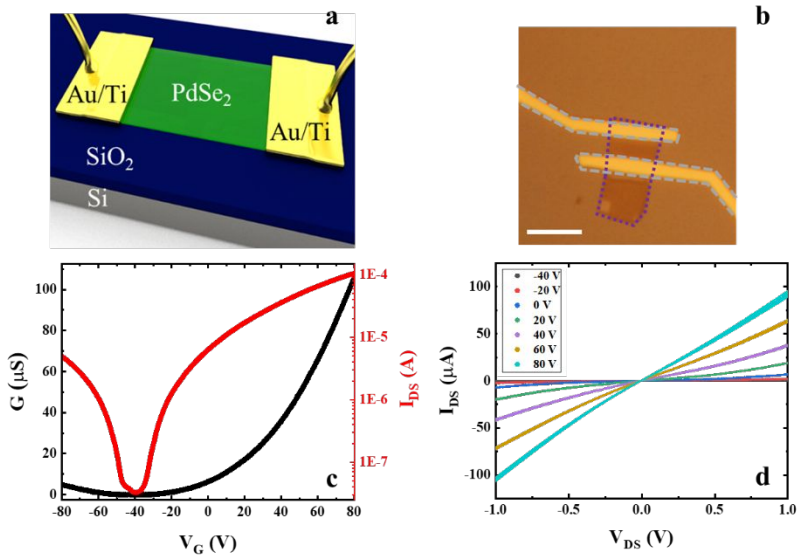

Figure 1. (a) A schematic and (b) optical micrograph of an as-fabricated typical $PdSe_2$ phototransistor with gold electrodes and $PdSe_2$ channel outlined in gray and purple dashed lines, respectively. The scale bar in (b) is five microns. (c) Gate-dependent electrical transport of the $PdSe_2$ phototransistor. (d) The output characteristics of the device at various gate voltages.

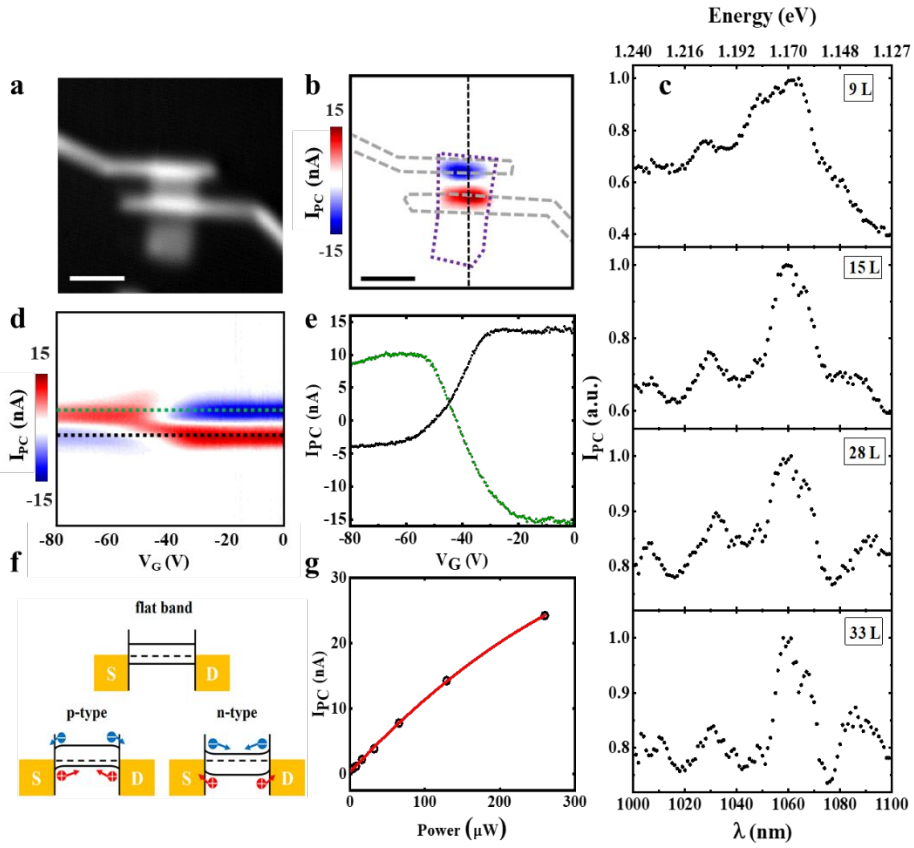

Figure 2. (a) Reflection and (b) scanning photocurrent images of a typical $PdSe_2$ phototransistor under 1060 nm illumination. Metal electrodes and few-layer $PdSe_2$ channel are outlined by gray and purple dashed lines, respectively. The scale bars are five microns. (c) Normalized wavelength-dependent photocurrent responses of $PdSe_2$ phototransistors with different thickness. (d) Gate-dependent photocurrent signals along the black dashed cutline in (b) with a zero drain-source bias. (e) Green and black curves represent photocurrent responses along the green and black dashed lines in (d), respectively. (f) Schematic diagrams for photocurrent generation mechanisms for $PdSe_2$ phototransistors when the Fermi level moves from the valence band to the conduction band. (g) Power-dependent photocurrent behavior of the device, where the red solid line shows the trend line of $I_{PC} \propto P^{\gamma}$with $\gamma = 0.85$.

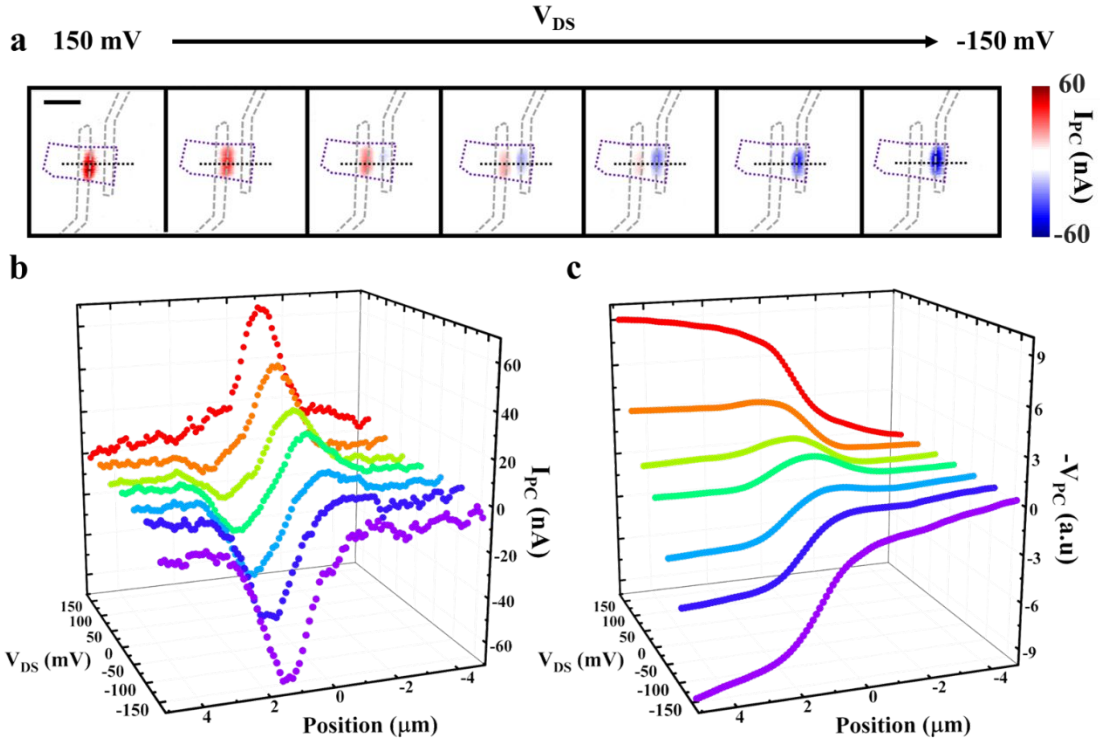

Figure 3. (a) Scanning photocurrent images (20 μm by 20 μm) with drain-source biases sweeping from -150 mV to 150 mV. The scale bar is five microns. (b) Corresponding photocurrent intensity along the black dashed lines in (a). (c) Electrostatic potential computed by numerically integrating the photocurrent intensity curves from (b).

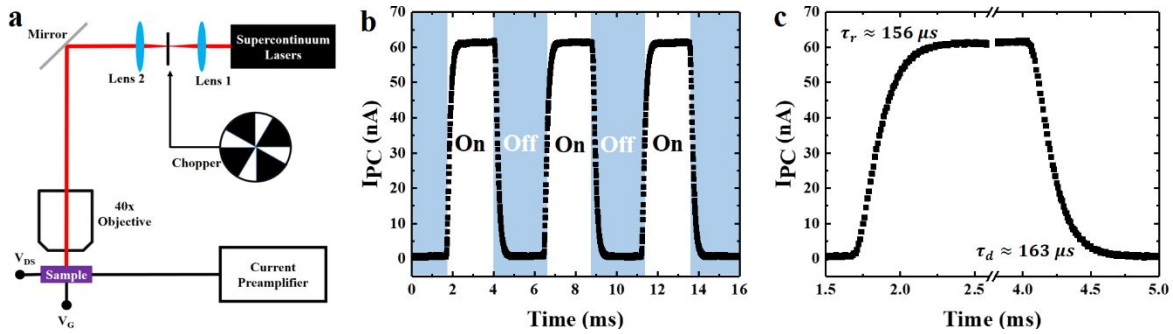

Figure 4. (a) Schematic of the setup used to perform temporally-resolved photocurrent measurements. (b) Photocurrent signals as a function of time under 1060 nm illumination. (c) Zoom-in of the rising and decaying regions of the photocurrent signals from (b) showing the rise and decay time constants of ~156 μs and ~163 μs, respectively.

References:

1. K. S. Novoselov, A. K. Geim, S. V. Morozov, D. Jiang, Y. Zhang, S. V. Dubonos, I. V. Grigorieva and A. A. Firsov, *Science*, 2004, **306**, 666.
2. K. S. Novoselov, D. Jiang, F. Schedin, T. J. Booth, V. V. Khotkevich, S. V. Morozov and A. K. Geim, *Proceedings of the National Academy of Sciences of the United States of America*, 2005, **102**, 10451-10453.
3. Q. H. Wang, K. Kalantar-Zadeh, A. Kis, J. N. Coleman and M. S. Strano, *Nature Nanotechnology*, 2012, **7**, 699.
4. B. Radisavljevic, A. Radenovic, J. Brivio, V. Giacometti and A. Kis, *Nature Nanotechnology*, 2011, **6**, 147.
5. T. Wang, K. Andrews, A. Bowman, T. Hong, M. Koehler, J. Yan, D. Mandrus, Z. Zhou and Y.-Q. Xu, *Nano Letters*, 2018, **18**, 2766-2771.
6. S. Das, H.-Y. Chen, A. V. Penumatcha and J. Appenzeller, *Nano Letters*, 2013, **13**, 100-105.
7. H. Wang, L. Yu, Y.-H. Lee, Y. Shi, A. Hsu, M. L. Chin, L.-J. Li, M. Dubey, J. Kong and T. Palacios, *Nano Letters*, 2012, **12**, 4674-4680.
8. O. Lopez-Sanchez, D. Lembke, M. Kayci, A. Radenovic and A. Kis, *Nature Nanotechnology*, 2013, **8**, 497.
9. Z. Yin, H. Li, H. Li, L. Jiang, Y. Shi, Y. Sun, G. Lu, Q. Zhang, X. Chen and H. Zhang, *Acs Nano*, 2012, **6**, 74-80.
10. H. Zeng, J. Dai, W. Yao, D. Xiao and X. Cui, *Nature Nanotechnology*, 2012, **7**, 490.
11. K. F. Mak, K. He, J. Shan and T. F. Heinz, *Nature Nanotechnology*, 2012, **7**, 494.
12. E. Zhang, Y. Jin, X. Yuan, W. Wang, C. Zhang, L. Tang, S. Liu, P. Zhou, W. Hu and F. Xiu, *Advanced Functional Materials*, 2015, **25**, 4076-4082.
13. M. Hafeez, L. Gan, H. Li, Y. Ma and T. Zhai, *Advanced Materials*, 2016, **28**, 8296-8301.
14. X. Yu, P. Yu, D. Wu, B. Singh, Q. Zeng, H. Lin, W. Zhou, J. Lin, K. Suenaga, Z. Liu and Q. J. Wang, *Nat Commun*, 2018, **9**, 1545.
15. L. Li, W. Wang, Y. Chai, H. Li, M. Tian and T. Zhai, *Advanced Functional Materials*, 2017, **27**, 1701011.
16. X. Liu, H. Zhou, B. Yang, Y. Qu and M. Zhao, *Sci Rep*, 2017, **7**, 39995.
17. A. D. Oyedele, S. Yang, L. Liang, A. A. Puretzky, K. Wang, J. Zhang, P. Yu, P. R. Pudasaini, A. W. Ghosh, Z. Liu, C. M. Rouleau, B. G. Sumpter, M. F. Chisholm, W. Zhou, P. D. Rack, D. B. Geohegan and K. Xiao, *Journal of the American Chemical Society*, 2017, **139**, 14090-14097.
18. D. Qin, P. Yan, G. Ding, X. Ge, H. Song and G. Gao, *Sci Rep*, 2018, **8**, 2764.
19. M. Sun, J.-P. Chou, L. Shi, J. Gao, A. Hu, W. Tang and G. Zhang, *ACS Omega*, 2018, **3**, 5971-5979.
20. J. Sun, H. Shi, T. Siegrist and D. J. Singh, *Appl Phys Lett*, 2015, **107**, 153902.
21. W. L. Chow, P. Yu, F. Liu, J. Hong, X. Wang, Q. Zeng, C.-H. Hsu, C. Zhu, J. Zhou, X. Wang, J. Xia, J. Yan, Y. Chen, D. Wu, T. Yu, Z. Shen, H. Lin, C. Jin, B. K. Tay and Z. Liu, *Advanced Materials*, 2017, **29**, 1602969.
22. X. Zhao, B. Qiu, G. Hu, W. Yue, J. Ren and X. Yuan, *Materials*, 2018, **11**, 2339.

23. Q. Liang, Q. Wang, Q. Zhang, J. Wei, S. X. Lim, R. Zhu, J. Hu, W. Wei, C. Lee, C. Sow, W. Zhang and A. T. S. Wee, *Advanced Materials*, 2019, **0**, 1807609.
24. S. R. Tamalampudi, Y.-Y. Lu, R. Kumar U, R. Sankar, C.-D. Liao, K. Moorthy B, C.-H. Cheng, F. C. Chou and Y.-T. Chen, *Nano Letters*, 2014, **14**, 2800-2806.
25. S. Das, H.-Y. Chen, A. V. Penumatcha and J. Appenzeller, *Nano Lett.*, 2012, **13**, 100-105.
26. T. Hong, B. Chamlagain, W. Lin, H.-J. Chuang, M. Pan, Z. Zhou and Y.-Q. Xu, *Nanoscale*, 2014, **6**, 8978-8983.
27. E. Li, D. Wang, P. Fan, R. Zhang, Y.-Y. Zhang, G. Li, J. Mao, Y. Wang, X. Lin, S. Du and H.-J. Gao, *Nano Research*, 2018, **11**, 5858-5865.
28. A. A. Puretzky, A. D. Oyedele, K. Xiao, A. V. Haglund, B. G. Sumpter, D. Mandrus, D. B. Geohegan and L. Liang, *2d Mater*, 2018, **5**, 035016.
29. T. Wang, S. Hu, B. Chamlagain, T. Hong, Z. Zhou, S. M. Weiss and Y.-Q. Xu, *Advanced Materials*, 2016, **28**, 7162-7166.
30. A. W. Tsen, L. A. K. Donev, H. Kurt, L. H. Herman and J. Park, *Nature Nanotechnology*, 2009, **4**, 108-113.
31. T. Hong, B. Chamlagain, S. Hu, S. M. Weiss, Z. Zhou and Y.-Q. Xu, *Acs Nano*, 2015, **9**, 5357-5363.
32. M. Buscema, M. Barkelid, V. Zwiller, H. S. J. van der Zant, G. A. Steele and A. Castellanos-Gomez, *Nano Letters*, 2013, **13**, 358-363.
33. M. Cutler and N. F. Mott, *Phys Rev*, 1969, **181**, 1336-&.
34. Y. M. Zuev, W. Chang and P. Kim, *Physical Review Letters*, 2009, **102**.
35. S. Rosenblatt, Y. Yaish, J. Park, J. Gore, V. Sazonova and P. L. McEuen, *Nano Letters*, 2002, **2**, 869-872.
36. X. Zhang, J. Jie, W. Zhang, C. Zhang, L. Luo, Z. He, X. Zhang, W. Zhang, C. Lee and S. Lee, *Advanced Materials*, 2008, **20**, 2427-2432.
37. Y. Liu, J. Guo, E. Zhu, L. Liao, S.-J. Lee, M. Ding, I. Shakir, V. Gambin, Y. Huang and X. Duan, *Nature*, 2018, **557**, 696-700.
38. H.-J. Chuang, B. Chamlagain, M. Koehler, M. M. Perera, J. Yan, D. Mandrus, D. Tománek and Z. Zhou, *Nano Letters*, 2016, **16**, 1896-1902.
39. X. Cui, E.-M. Shih, L. A. Jauregui, S. H. Chae, Y. D. Kim, B. Li, D. Seo, K. Pistunova, J. Yin, J.-H. Park, H.-J. Choi, Y. H. Lee, K. Watanabe, T. Taniguchi, P. Kim, C. R. Dean and J. C. Hone, *Nano Letters*, 2017, **17**, 4781-4786.
40. M. Bass, *Handbook of Optics: Devices, Measurements, and Properties*, McGraw-Hill Professoinal, 1994.